Check for updates

Research Article Vol. 26, No. 2 | 22 Jan 2018 | OPTICS EXPRESS 1942

Optics EXPRESS

Terahertz master-oscillator power-amplifier quantum cascade laser with a grating coupler of extremely low reflectivity

HUAN ZHU,[1,2] HAIQING ZHU,[1,2] FANGFANG WANG,[1] GAOLEI CHANG,[1,2] CHENREN YU,[1,2] QUAN YAN,[1] JIANXIN CHEN,[1] LIANHE LI,[3] A. GILES DAVIES,[3] EDMUND H. LINFIELD,[3] ZHOU TANG,[4] PINGPING CHEN,[4] WEI LU,[4] GANGYI XU,[1,*] AND LI HE[1]

[1]*Key Laboratory of Infrared Imaging Materials and Detectors, Shanghai Institute of Technical Physics, Chinese Academy of Sciences, Shanghai 200083, China*
[2]*University of Chinese Academy of Sciences, Beijing 100049, China*
[3]*School of Electronic and Electrical Engineering, University of Leeds, Leeds LS2 9JT, United Kingdom*
[4]*National Laboratory of Infrared Physics, Shanghai Institute of Technical Physics, Chinese Academy of Sciences, Shanghai 200083, China*
**gangyi.xu@mail.sitp.ac.cn*

Abstract: A terahertz master-oscillation power-amplifier quantum cascade laser (THz-MOPA-QCL) is demonstrated where a grating coupler is employed to efficiently extract the THz radiation. By maximizing the group velocity and eliminating the scattering of THz wave in the grating coupler, the residue reflectivity is reduced down to the order of 10^{-3}. A buried DFB grating and a tapered preamplifier are proposed to improve the seed power and to reduce the gain saturation, respectively. The THz-MOPA-QCL exhibits single-mode emission, a single-lobed beam with a narrow divergence angle of 18° × 16°, and a pulsed output power of 136 mW at 20 K, which is 36 times that of a second-order DFB laser from the same material.

OCIS codes: (140.3280) Laser amplifiers; (140.3490) Lasers, distributed-feedback; (140.5965) Semiconductor lasers, quantum cascade; (300.6495) Spectroscopy, terahertz.

References and links

1. M. Tonouchi, "Cutting-edge terahertz technology," Nat. Photonics **1**(2), 97–105 (2007).
2. P. U. Jepsen, D. G. Cooke, and M. Koch, "Terahertz spectroscopy and imaging – Modern techniques and applications," Laser Photonics Rev. **5**(1), 124–166 (2011).
3. A. J. Fitzgerald, E. Berry, N. N. Zinovev, G. C. Walker, M. A. Smith, and J. M. Chamberlain, "An introduction to medical imaging with coherent terahertz frequency radiation," Phys. Med. Biol. **47**(7), R67–R84 (2002).
4. J. Federici and L. Moeller, "Review of terahertz and subterahertz wireless communications," J. Appl. Phys. **107**(11), 111101 (2010).
5. H. T. Chen, R. Kersting, and G. C. Cho, "Terahertz imaging with nanometer resolution," Appl. Phys. Lett. **83**(15), 3009–3011 (2003).
6. A. W. M. Lee, Q. Qin, S. Kumar, B. S. Williams, Q. Hu, and J. L. Reno, "Real-time terahertz imaging over a standoff distance (> 25 meters)," Appl. Phys. Lett. **89**(14), 141125 (2006).
7. R. Köhler, A. Tredicucci, F. Beltram, H. E. Beere, E. H. Linfield, A. G. Davies, D. A. Ritchie, R. C. Iotti, and F. Rossi, "Terahertz semiconductor-heterostructure laser," Nature **417**(6885), 156–159 (2002).
8. M. S. Vitiello, G. Scalari, B. Williams, and P. De Natale, "Quantum cascade lasers: 20 years of challenges," Opt. Express **23**(4), 5167–5182 (2015).
9. B. S. Williams, "Terahertz quantum-cascade lasers," Nat. Photonics **1**(9), 517–525 (2007).
10. C. Sirtori, S. Barbieri, and R. Colombelli, "Wave engineering with THz quantum cascade lasers," Nat. Photonics **7**(9), 691–701 (2013).
11. A. Mottaghizadeh, D. Gacemi, P. Laffaille, H. Li, M. Amanti, C. Sirtori, G. Santarelli, W. Hansel, R. Holzwart, L. H. Li, E. H. Linfield, and S. Barbieri, "5-ps-long terahertz pulses from an active-modelocked quantum cascade laser," Optica **4**, 168–171 (2017).
12. G. Scalari, C. Walther, M. Fischer, R. Terazzi, H. Beere, D. Richie, and J. Faist, "THz and sub-THz quantum cascade lasers," Laser Photonics Rev. **3**(1-2), 45–66 (2009).

#313356 https://doi.org/10.1364/OE.26.001942
Journal © 2018 Received 13 Nov 2017; revised 14 Jan 2018; accepted 16 Jan 2018; published 18 Jan 2018

13. B. Paulillo, S. Pirotta, H. Nong, P. Crozat, S. Guilet, G. Xu, S. Dhillon, L. H. Li, A. G. Davies, E. H. Linfiled, and R. Colombelli, "Ultrafast terahertz detectors based on three-dimensional meta-atoms," Optica **4**(12), 1451–1456 (2017).
14. T. Y. Kao, J. L. Reno, and Q. Hu, "Phase-locked laser arrays through global antenna mutual coupling," Nat. Photonics **10**(8), 541–546 (2016).
15. L. Xu, D. Chen, C. A. Curwen, M. Memarian, J. L. Reno, T. Itoh, and B. S. Williams, "Metasurface quantum-cascade laser with electrically switchable polarization," Optica **4**(4), 468–475 (2017).
16. A. Khalatpour, J. L. Reno, N. P. Kherani, and Q. Hu, "Unidirectional photonic wire laser," Nat. Photonics **11**(9), 555–559 (2017).
17. S. Schönhuber, M. Brandstetter, T. Hisch, C. Deutsch, M. Krall, H. Detz, A. M. Andrews, G. Strasser, S. Rotter, and K. Unterrainer, "Random lasers for broadband directional emission," Optica **3**(10), 1035–1038 (2016).
18. M. I. Amanti, M. Fischer, G. Scalari, M. Beck, and J. Faist, "Low-divergence single-mode terahertz quantum cascade laser," Nat. Photonics **3**(10), 586–590 (2009).
19. G. Xu, R. Colombelli, S. P. Khanna, A. Belarouci, X. Letartre, L. Li, E. H. Linfield, A. G. Davies, H. E. Beere, and D. A. Ritchie, "Efficient power extraction in surface-emitting semiconductor lasers using graded photonic heterostructures," Nat. Commun. **3**, 952 (2012).
20. G. Xu, Y. Halioua, S. Moumdji, R. Colombelli, H. E. Beere, and D. A. Ritchie, "Stable single-mode operation of surface-emitting terahertz lasers with graded photonic heterostructure resonators," Appl. Phys. Lett. **102**(23), 231105 (2013).
21. G. Xu, L. Li, N. Isac, Y. Halioua, A. Giles Davies, E. H. Linfield, and R. Colombelli, "Surface-emitting terahertz quantum cascade lasers with continuous-wave power in the tens of milliwatt range," Appl. Phys. Lett. **104**(9), 091112 (2014).
22. J. N. Walpole, "Semiconductor amplifier and lasers with tapered gain regions," Opt. Quantum Electron. **28**(6), 623–645 (1996).
23. S. O'Brien, R. Lang, R. Parke, J. Major, D. F. Welch, and D. Mehuys, "2.2-W Continuous-Wave Diffraction-Limited Monolithically Integrated Master Oscillator Power Amplifier at 854 nm," IEEE Photonics Technol. Lett. **9**(4), 440–442 (1997).
24. K. Kim, S. Lee, and P. Delfyett, "1.4kW high peak power generation from an all semiconductor mode-locked master oscillator power amplifier system based on eXtreme Chirped Pulse Amplification(X-CPA)," Opt. Express **13**(12), 4600–4606 (2005).
25. H. Wenzel, K. Paschke, O. Brox, F. Bugge, J. Fricke, A. Ginolas, A. Knauer, P. Ressel, and G. Erbert, "10 W continuous-wave monolithically integrated master-oscillator power-amplifier," Electron. Lett. **43**(3), 160–161 (2007).
26. M. Troccoli, C. Gmachl, F. Capasso, D. L. Sivco, and A. Y. Cho, "Mid-infrared (λ≈7.4 μm) quantum cascade laser amplifier for high power single-mode emission and improved beam quality," Appl. Phys. Lett. **80**(22), 4103–4105 (2002).
27. P. Rauter, S. Menzel, A. K. Goyal, B. Gökden, C. A. Wang, A. Sanchez, G. W. Turner, and F. Capasso, "Master-oscillator power-amplifier quantum cascade laser array," Appl. Phys. Lett. **101**(26), 261117 (2012).
28. B. Hinkov, M. Beck, E. Gini, and J. Faist, "Quantum cascade laser in a master oscillator power amplifier configuration with Watt-level optical output power," Opt. Express **21**(16), 19180–19186 (2013).
29. P. Rauter and F. Capasso, "Multi-wavelength quantum cascade laser arrays," Laser Photonics Rev. **9**(5), 452–477 (2015).
30. C. Mauro, R. P. Green, A. Tredicucci, F. Beltram, H. E. Beere, and D. A. Ritchie, "Amplification of terahertz radiation in quantum cascade structures," J. Appl. Phys. **102**(6), 063101 (2007).
31. Y. Ren, R. Wallis, Y. D. Shah, D. S. Jessop, R. Degl'Innocenti, A. Klimont, V. Kamboj, H. E. Beere, and D. A. Ritchie, "Single mode terahertz quantum cascade amplifier," Appl. Phys. Lett. **105**(14), 141102 (2014).
32. H. Zhu, F. F. Wang, Q. Yuan, C. R. Yu, J. X. Chen, G. Xu, L. He, L. H. Li, L. Chen, A. G. Davies, E. H. Linfield, J. M. Hao, P. B. Vigneron, and R. Colombelli, "Terahertz master-oscillator power-amplifier quantum cascade lasers," Appl. Phys. Lett. **109**(23), 231105 (2016).
33. M. I. Amanti, G. Scalari, R. Terazzi, M. Fischer, M. Beck, J. Faist, A. Rudra, P. Gallo, and E. Kapon, "Bound-to-continuum terahertz quantum cascade laser with a single-quantum-well phonon extraction/injection stage," New J. Phys. **11**(12), 125022 (2009).

1. Introduction

Terahertz (THz) frequency radiation (loosely defined to span the 1–10 THz frequency range) has important applications ranging from spectroscopy, imaging, through to wireless communications [1–6]. The study of terahertz quantum cascade lasers (THz-QCLs) has attracted increasing interest since they are the only compact THz coherent source with the brightest radiation and can be ultra-fast modulated [7–13]. However, it is a long standing challenge to improve the output power and the beam directionality of the THz-QCLs, mainly due to the severe mismatching between the mode highly confined in the sub-wavelength (at least in one direction) cavity and the mode in the free space. Some unique photonic concepts have been developed to address this issue [14–21]. Among these efforts, a power extractor with designable reflectivity and radiation efficiency is highly desired to link the tiny cavity and the free space, and it is particularly important when we try to monolithically integrate a master-oscillator power-amplifier (MOPA) architecture in the THz-QCL.

MOPA is a promising configuration to improve output power and beam quality of semiconductor lasers [22–29]. In an MOPA laser, the seed radiation generated in the master-oscillator (MO) section is efficiently injected into the power-amplifier (PA) section and, after amplification, is coupled out from the front facet of the latter. In order to fully exploit the material gain and enhance the power amplification, it is crucial to suppress self-lasing in the PA section. To this target, the facet reflectivity in the PA section needs to be as low as ~0.1%. In the near- and mid-infrared frequency range, such low reflectivity can be realized by depositing high quality antireflection (AR) multilayers, with the assistance of facet tilting [22]. However, in the THz frequency range, due to the very long wavelength, high quality AR layers are still not available, which has for a long time obstructed the realization of the MOPA architecture in THz-QCLs [30,31].

Until recently did we demonstrate the first terahertz master-oscillator power-amplifier quantum cascade laser (THz-MOPA-QCL), where a grating coupler instead of AR layers is exploited to extract the THz radiation [32]. Stable single-mode emission has been demonstrated, and the factor of power amplification was about 5. However, the absolute output power achieved in that work was very limited (~1.3 mW), and the main reason is the considerable residue reflection caused by the grating coupler which constrains the length of the preamplifier and thus degrades the effect of power amplification. Moreover, the metallic DFB grating used in the MO section leads to a high contrast of the refractive index and hence a strong mode confinement, which results in a low seed power.

In this work, we reveal that the reflection induced by the grating coupler originates from two mechanisms – the intrinsic reflection caused by the periodic contrast of the refractive index in the grating coupler, and the parasitic reflection caused by the scattering from the lateral ends of the grating coupler. Here, we propose a new design of the grating coupler to minimize both the intrinsic and the parasitic reflection, and finally reduce the total reflectivity down to the order of 10^{-3}. In addition, a buried DFB grating with controllable index contrast is employed, which efficiently increases the seed power from the MO section. A tapered preamplifier is proposed to reduce the gain saturation. All these innovations result in a single-mode emission THz-MOPA-QCL with an output power of 136 mW, which is ~100 times that of the previous MOPA devices (from a different material), and is 36 times that of conventional single-mode second-order DFB lasers, and is even 16 times that of the multimode Fabry-Perot (FP) lasers fabricated from the same material.

2. Device concept and modeling

Figure 1(a) shows the scheme of a THz-MOPA-QCL. The GaAs/$Al_{0.15}Ga_{0.85}As$ active region used in this work is based on a bound-to-continuum design [33], with a thickness of ~13 μm and a measured central emission frequency of ~2.6 THz. The device is based on a metal-metal waveguide. The MO section is a first-order DFB laser featuring a buried DFB grating with a central π-phase-shift, in which the periodic grooves are formed on the top of active region by wet etching and then are covered by the top metallization. The PA section consists of a straight preamplifier, a grating coupler and an absorbing boundary. The grating coupler – sufficiently wider than the preamplifier – consists of periodic air slits in the top metallization, extracting the THz wave from the PA section into the free space. The absorbing boundary is constructed via the highly doped n^+ GaAs top contact layer which is not covered by the top metallization. A part of the THz wave will transmit through the grating coupler and then annihilate in the absorbing boundary.

Figure 1(b) shows the photonic band structures of the DFB grating and the grating coupler. In the MO section, the operating mode is the defect state – caused by the central π-phase-shift – inside the band gap and its frequency is marked as ω_0. To minimize the intrinsic reflection, the grating coupler is designed so that the state with frequency ω_0 locates in the energy band above the second band gap, and its group velocity ($\left.\frac{\partial\omega}{\partial k_x}\right|_{\omega=\omega0}$) is near the maximum. Here, ω and k_x are respectively the frequency and wave vector in the photonic band structure. High group velocity indicates weak feedback and thus low reflectivity. By assuming that the grating coupler is infinitely wide and using 2D full wave finite element method (FEM, solver COMSOL Multiphysics), we calculated the intrinsic reflectivity caused by the grating coupler in the frequency range of the material gain. The results are plotted as the black squares in Fig. 2, showing that the intrinsic reflectivity is about or even less than 0.1%.

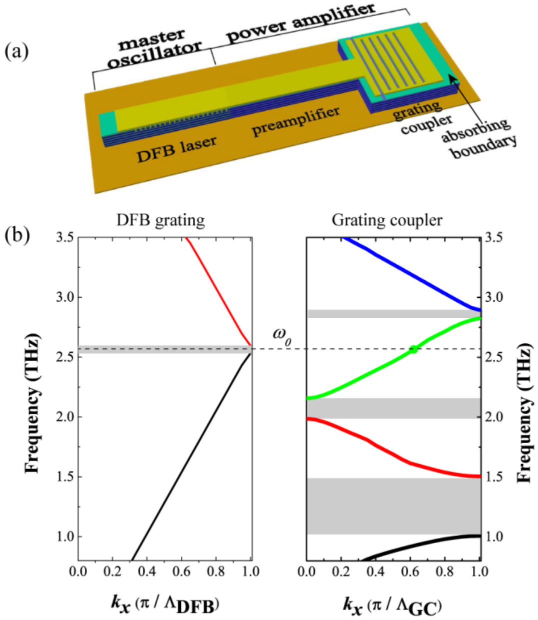

Fig. 1. (a) Schematic illustration of a THz-MOPA-QCL based on a metal-metal waveguide. (b) The photonic band structures for the DFB grating and the grating coupler. The gray zones correspond to the band gaps, and the dashed line shows the lasing frequency (ω_0). The DFB mode (the defect state inside the band gap) in the MO is aligned with a state in the third band in the grating coupler, whose group velocity is near the maximum. The periodicities of the DFB grating (Λ_{DFB}) and the grating coupler (Λ_{GC}) are respectively 16.2 µm and 46.0 µm.

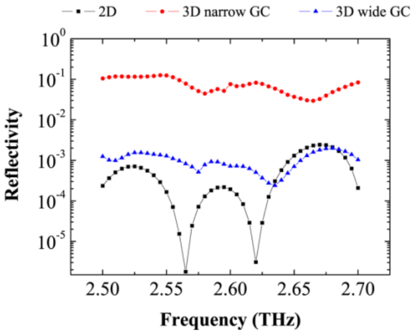

Fig. 2. Calculated reflectivity caused by the grating coupler. The black squares are the 2D simulation results which correspond to the intrinsic reflectivity. The red circles are 3D results where the grating coupler and the preamplifier are 150 µm in width. The blue triangles are 3D

results where the grating coupler is 600-μm-wide while the preamplifier is 150-μm-wide. GC means grating coupler.

However, for a practical grating coupler with finite width, the spatial overlap between its lateral ends and the THz field will cause scattering and result in parasitic reflection. Figures 3(a) and 3(b) compare the propagation of THz wave (the frequency is 2.6 THz) in two different PA sections calculated by 3D FEM simulations, where the preamplifiers are 150-μm-wide, and the width of the grating couplers are respectively 150 μm and 600 μm. In the structure where the grating coupler is as narrow as the preamplifier [Fig. 3(a)], the considerable scattering leads the total reflectivity to be 7.6×10^{-2}. When the grating coupler is sufficient wider than the preamplifier [Fig. 3(b)], the spatial overlap and thus the scattering is efficiently eliminated, and the total reflectivity is as low as 7.2×10^{-4}. Figure 2 also shows the frequency spectra of the total reflectivity for the two PA sections. In the considered frequency range, the PA with a widened grating coupler exhibits low total reflectivity (blue triangles) which is close to the intrinsic reflectivity, and is nearly two orders of magnitude lower than that (red circles) of the PA with a narrow grating coupler. It indicates that the parasitic reflection is of dominant importance for the design of low-reflectivity grating coupler. Thanks to the gain ($g \approx 25$ cm^{-1}) of the active region embedded in the grating coupler, the power flux extracted from the grating coupler is about 1.25 times that injected into the grating coupler. These calculations reveal that the grating coupler developed in this work can efficiently extract the THz radiation from the MOPA with a residue reflectivity in the order of 10^{-3}.

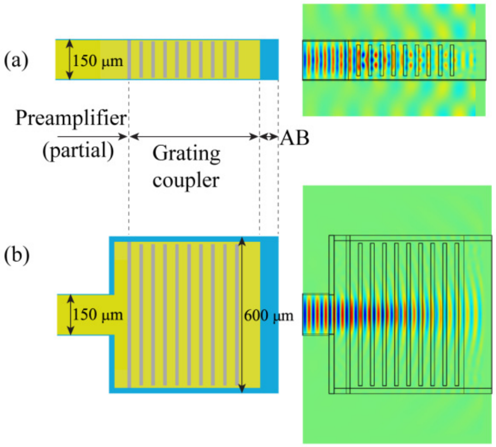

Fig. 3. The left panels of (a) and (b) show the schemes of two PA sections, where the preamplifier is 150-μm-wide but the grating couplers are 150 μm and 600 μm in width, respectively. The right panels show the field distribution when THz wave propagates through the preamplifier into the grating coupler in the two structures. In both structures, the grating coupler contains 10 periods, the periodicity is 46.0 μm and the air slit is 10.0-μm-wide. AB is the absorbing boundary.

The index contrast in the buried DFB grating can be flexibly controlled by the etching depth. Manipulating the etching depth and the number of periods in the buried DFB grating, we can simultaneously optimize the injected power and the radiation efficiency of the MO section, and thus maximize the seed power. By finite-difference time-domain (FDTD) simulations, we calculated the mode profile ($|E_z|^2$) in the MO with an optimized buried DFB grating, and the result is given in Fig. 4(a). The buried DFB grating contains 80 periods with a central π-phase-shift, the grating periodicity and the duty cycle are respectively 16.2 μm and 75%, and the grating depth is 0.5 μm. Figure 4(a) shows that the ratio of light intensity at the export to the maximum intensity inside the MO is about 38%, indicating high radiation efficiency. As a comparison, in Fig. 4(b) we plot the mode profile in the MO with a metallic

DFB grating utilized in our previous work, in which the grating is formed by the air slits in the top metallization and it contains only 30 periods [32]. In the latter case, the corresponding ratio is as low as ~5.5%, meaning very low radiation efficiency. Such comparison is also supported by the analysis of the radiation loss (α_{rad}) and the injected power ($P_{in,MO}$) of the MO section. The calculated α_{rad} is 5.4 cm^{-1} for the MO with a buried grating, lager than the value (3.0 cm^{-1}) for the one with a metallic grating, but is sufficiently lower than the material loss (α_{mat}) of the metal-metal waveguide which is about 15-20 cm^{-1} [9]. The input power of the former, proportional to the length of the DFB grating, is about 2.8 times that of the latter. Since the seed power ($P_{out,MO}$) is proportional to $P_{in,MO} \times \alpha_{rad} / (\alpha_{rad} + \alpha_{mat})$, the MO section with a buried DFB grating will increase the seed power by a fact of ~5.0, compared with the one with a metallic grating.

It should be noted that α_{rad} influences the threshold current, the slope efficiency, and the lasing dynamic range of the MO section. A careful balance between α_{rad} and $P_{in,MO}$ will further improve the seed power of the MO section.

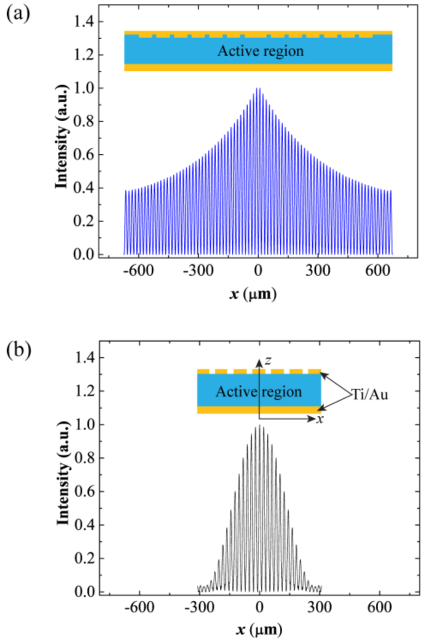

Fig. 4. THz wave intensity distribution ($|E_z|^2$) along a line through the center of the MO section with a buried DFB grating (a), or a metallic DFB grating (b). The insets show the schematic cross-sections of the buried and the metallic DFB gratings, respectively.

3. Experiment results of THz-MOPA-QCLs with a straight preamplifier

Based on the aforementioned design, THz-MOPA-QCLs with different structure parameters have been systemically fabricated. The periodicity of the DFB grating (Λ_{DFB}) varies from 16.0 to 16.6 μm, the width of MO section and the straight preamplifier are set as 150 μm, and the length of the preamplifier varies from 100 μm to 1500 μm. The grating coupler is 600 μm in width and contains 10 periods, and several different periodicities (46 μm, 48 μm, and 50 μm) have been tested. The top metallization of the MO section and the preamplifier are linked with each other. There is an air gap in the top metallization – between the preamplifier and the grating coupler – whose position and width are designed so that the air gap acts as the first air slit in the grating coupler. Consequently, the grating coupler can be separately pumped, but the THz wave will not be disturbed.

The GaAs/AlGaAs epilayers of the THz-QCL were grown on a semi-insulator GaAs substrate via molecular beam epitaxy (MBE). After epitaxy, the sample surface together with an n$^+$ GaAs holder wafer is Ti/Au coated. The sample carrier is glued on the holder wafer via thermo-compressive Au-Au bonding. The semi-insulator GaAs substrate is then removed via mechanical polishing followed by selective wet-etching. Once the GaAs/AlGaAs epitaxy is uncovered, the top n$^+$ GaAs (200 nm in thickness) contact layer is partially removed by wet etching. After that, the DFB grating is formed on the top of the active region by another wet etching, and the etching depth is about 500 nm controlled by a surface profiler (Dektak 150). The top metallization is then formed on the top of the active region, defined by contact photolithography, e-beam evaporation, and lift-off. The DFB grating in the MO section is covered by the top metallization, giving rise to a buried DFB grating. The grating coupler is also formed in this step via defining periodic air slits in the top metallization in the PA section. The top n$^+$ GaAs layer left in place, which is not covered by the top metallization, forms the absorbing boundary. Later, the device ridge is defined by chlorine-based inductively coupled plasma (ICP) etching. Finally, the back-side process consists of substrate thinning, Ti/Au evaporation and sample cutting via micro-dicing with a diamond blade. Figure 5(a) shows an SEM picture of a THz-MOPA-QCL with a straight preamplifier.

The fabricated devices are In-soldered on a Cu heat sink and mounted on the cold finger of a close-cycle cryostat. The spectra, light–current and current–voltage characteristics were measured in pulsed mode (the repeat frequency is 40 kHz and the pulse width is 1 μs). The spectral characteristics were measured using a Fourier transform infrared spectrometer (Bruker 80V) with a spectral resolution of 0.1 cm^{-1}. The emitted power was measured by a Golay cell which was calibrated by a Thomas Keating absolute terahertz power-meter. For the power measurement, only the readout of the detector is recorded, without taking into account the collection efficiency of the light branch or the transmissivity of the THz window in the cryostat. The far-field emission patterns of the devices were measured at 20 K with a Golay cell detector, which was scanned on a 15-cm-radius sphere centered on the device surface.

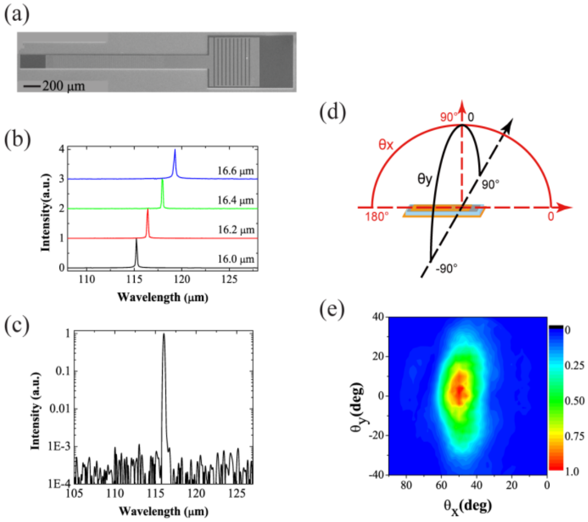

Fig. 5. (a) SEM picture of a THz-MOPA-QCL with a straight preamplifier. (b) Emission spectra of 4 THz-MOPA-QCL devices in which the periodicity of DFB grating varies from 16.0 to 16.6 μm. (c) Emission spectrum of a typical MOPA device showing that the side mode suppression ration (SMSR) is about 30 dB. (d) Schematic diagram defining the scanning angles used in beam profiling measurements. The angle $\theta_x = \theta_y = 0$ corresponds to the direction along the laser ridge. (e) Measured far-field pattern of a MOPA device where the preamplifier is 1500 μm in length.

Figure 5(b) displays the emission spectra of devices with different Λ_{DFB}, where all sections of the device were equally pumped at the level of maximum output power. The devices exhibit single-mode emission, and the emission wavelength varies linearly from 115.4 µm to 119.5 µm when Λ_{DFB} varies from 16.0 µm to 16.6 µm. Moreover, the emission wavelength is independent of the structure parameters used in the preamplifier and the grating coupler, which confirms that the devices operate on the DFB mode activated in the MO section. In all the devices, even when the preamplifier is as long as 1500 µm, single-mode emission remains in the whole dynamic range of lasing and the side mode suppression ratio (SMSR) is about 30 dB. Figure 5(c) is a typical emission spectrum, where the preamplifier is 1500 µm in length. We would like to emphasis that in the measured frequency range, when the periodicity of the grating coupler changes from 46 µm to 50 µm, no self-lasing was observed in the PA section, confirming the robustness of the design of low-reflectivity grating coupler. This is mainly because that for a given grating coupler – as shown in Fig. 1(b) – the group velocity of optical mode keeps large in a wide frequency range.

Figure 5(d) shows the schematic geometry for the far-field measurement. The $\theta_x = \theta_y = 0$ angle corresponds to the direction along the laser ridge. Figure 5(e) shows the measured far-field beam of a MOPA device, which features a single-lobed pattern. The emission direction of the highest brightness is ~48° deviated from the plane of the device surface, and the full width at half maximum (FWHM) of the beam pattern is ~17° × 32°.

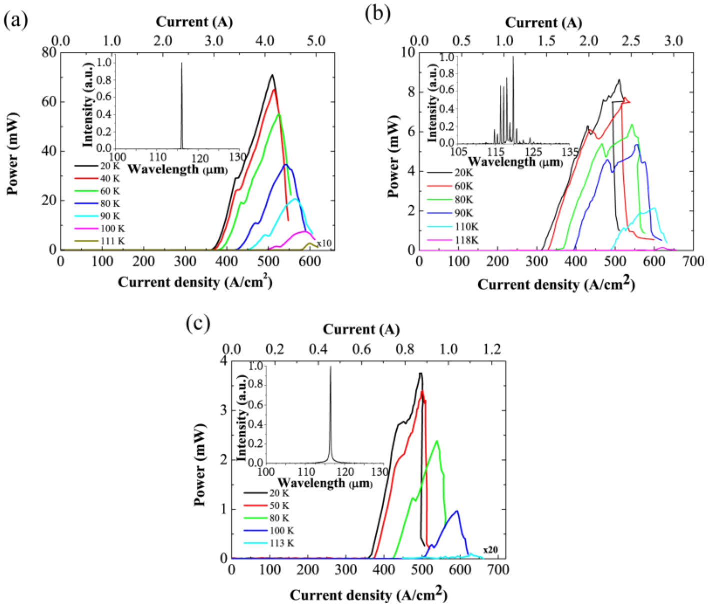

Fig. 6. Power-current density (*L*-*J*) curves measured at different heat-sink temperature for a THz-MOPA-QCL device with a 1500-µm-long straight preamplifier (a), a FP laser (b), and a second-order DFB laser (c). The maximum operation temperature for these 3 devices is 111 K, 118 K, and 113 K, respectively. The insets are the related emission spectra measured at 20 K. All devices are fabricated from the same chip and measured in pulsed mode (40 kHz repeat frequency, 1 µs pulse width).

The light-current density (*L*-*J*) curves at different heat-sink temperature of a typical THz-MOPA-QCL are presented in Fig. 6(a). The periodicity of the DFB grating is 16.2 µm, the straight preamplifier is 1500 µm in length, and the periodicity of the grating coupler is 46.0 µm, the emission wavelength is ~116.0 µm. The whole surface area of the device is 0.82 mm^2. The maximum output power of the MOPA device reaches to 71 mW at 20 K. The corresponding slope efficiency and wall-plug efficiency at 20 K are 87.6 mW/A and 0.16%, respectively. For performance comparison, we also fabricated in the same chip FP lasers and second-order DFB lasers, all based on a metal-metal waveguide. The *L-J* curves of a representative FP laser and a second-order DFB laser, measured under the same conditions, are shown in Figs. 6(b) and 6(c). The FP laser is 220 µm in width and 2.1 mm in length. The second-order DFB laser is 140-µm-wide and 1.4-mm-long, and the DFB grating contains 45 periods which is optimized according to our previous work [19]. The emission wavelength of the second-order DFB laser is 116.4 µm, which is near the peak of material gain and is close to that of the MOPA presented in Fig. 6(a). Figure 6(b) illustrates that the FP laser exhibits a peak power of 8.7 mW, a slope efficiency of 11.7 mW/A, and a wall-plug efficiency of 0.035% at 20 K. The corresponding values for the second-order DFB laser are 3.8 mW, 21.4 mW/A, and 0.041%, respectively. The output power of the MOPA device is far beyond those of the FP and the second-order DFB lasers, so do the slope efficiency and the wall-plug efficiency. Note, although the surface area of the MOPA device is larger than the other two, the output power of the FP and the second-order DFB lasers does not scale linearly with the device area.

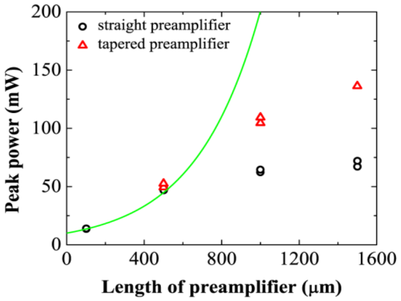

Fig. 7. Relationship between the peak power and the length of preamplifier for MOPA devices with straight or tapered preamplifiers. All devices have the same MO and grating coupler structures. The periodicities of the DFB grating and the grating coupler are 16.2 µm and 46.0 µm, respectively. All devices were measured at 20 K in pulsed mode (40 kHz repeat frequency, 1 µs pulse length). During the measurement, all sections of the MOPA device were equally pumped.

To investigate the effect of power amplification in the MOPA devices, we measured the peak output power (P_{out}) of the device as a function of the preamplifier length (L_{pre}), and the results are shown as the black circles in Fig. 7. The increase of P_{out} deviates significantly from the exponential function $P_{out} \propto \exp(g \times L_{pre})$, where g is the net gain of the preamplifier. Especially, P_{out} almost keeps constant when $L_{pre} \geq 1000$ µm. The phenomena strongly indicate the existence of gain saturation when we increase the length of the preamplifier.

4. Reduce the gain saturation

In order to reduce the gain saturation, we have also fabricated in the same chip THz-MOPA-QCLs with a tapered preamplifier. When THz wave propagates from the narrow to the wide port of the tapered preamplifier, the beam laterally spreads which will decrease the intensity density of the THz beam and thus reduce the gain saturation. Figures 8(a) and 8(b) show respectively a schematic and an SEM image of the new MOPA device. Note, the design of the MO and the grating coupler is the same for the MOPA with a straight or a tapered preamplifier. Three different lengths of the tapered preamplifier (500, 1000 and 1500 µm) have been tested, and the full taper angle is about 9°. The taper angle was chosen to enable an efficient utilization of the gain media. On the other hand, the grating coupler is still considerably wider than the tapered preamplifier in order to reduce the reflection. The detailed structure parameters of an MOPA device with a tapered preamplifier are described in the caption of Fig. 8.

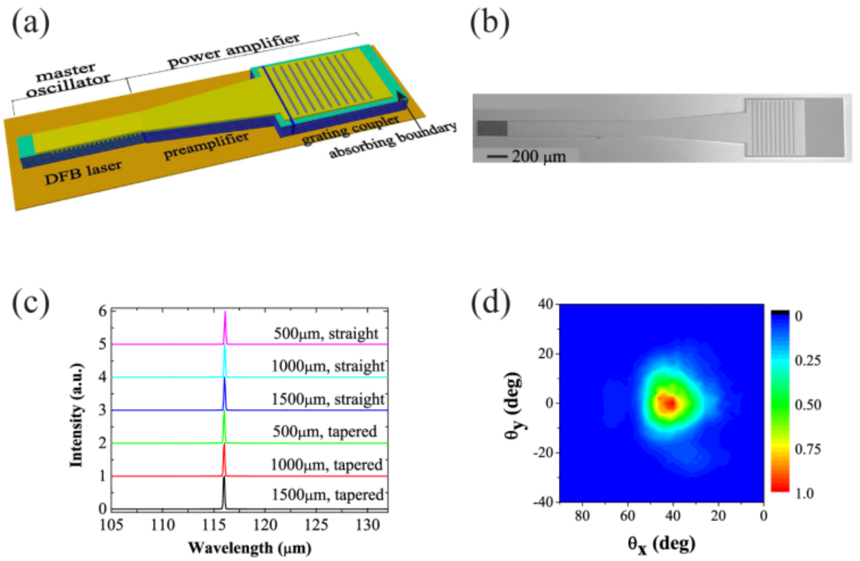

Fig. 8. (a) Schematic diagram of a THz-MOPA-QCL with a tapered preamplifier. (b) SEM picture of a MOPA device with a tapered preamplifier. The buried DFB grating in the MO section is 150 μm in width, and contains 80 periods with a central π-phase-shift. The grating coupler is 600 μm in width, and contains 10 periods with a periodicity of 46.0 μm. The preamplifier is 1000 μm in length and the full taper angle is 9°. (c) Emission spectra of a set of MOPA devices with straight or tapered preamplifiers. For all devices, the periodicities of the DFB grating and the grating coupler are respectively 16.2 μm and 46.0 μm. The length and the type of the preamplifier are marked in the figure. (d) Far-field beam pattern of a MOPA device with a tapered preamplifier whose length is 1500 μm.

Figure 8(c) shows the emission spectra of the MOPA devices with the straight or the tapered preamplifiers, where the MO section and the grating coupler are exactly the same. All the devices exhibit the same emission wavelength, demonstrating that the lasing is only seeded by the MO section. A tapered preamplifier, however, broadens the THz wave and increases the emission aperture which results in a more directional beam pattern. As shown in Fig. 8(d), the divergence angle of the MOPA device with a tapered preamplifier is ~18° × 16°. Figure 9 shows the *L-J-V* curves of an MOPA device with a tapered preamplifier whose length is 1500 μm, measured at different temperature in pulsed mode. At 20 K, the output power of the MOPA device peaks at 136 mW, the related slope efficiency and wall-plug efficiency are 143.6 mW/A and 0.28%, respectively. The peak output power remains 53.4 mW at 80 K, and the maximum operation temperature reaches 110 K. Compared with the FP laser and the second-order DFB laser fabricated from the same chip [see Figs. 6(b) and 6(c)], the MOPA device exhibits much higher output power, which is 36 times that of the second-order DFB laser, and is 16 times that of the multimode FP laser (all measured at 20 K with the same pulse driving conditions). The wall-plug efficiency of the MOPA device is also significantly higher than the other two kinds of lasers. It is worth noting that the superior power behaviors of the MOPA device are achieved without losing other characteristics such as the maximum operation temperature in pulsed mode.

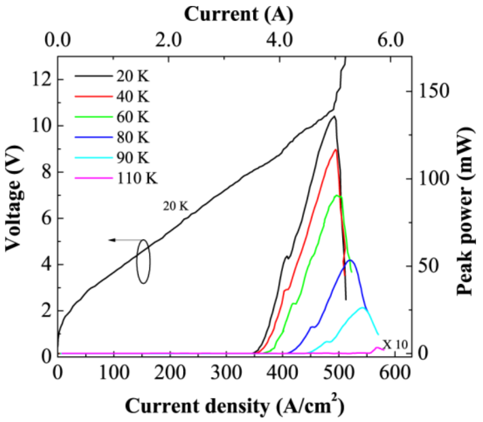

Fig. 9. *L-J-V* curves of an MOPA device with a tapered preamplifier measured at different operation temperature in pulsed mode. The repeat frequency of the current pulse is 40 kHz, and the pulse width is 1 μs. The length of the preamplifier is 1500 μm.

We now reconsider the effect of gain saturation and its influence on the power amplification. We measured the peak output power P_{out} of the MOPA devices as a function of the length (L_{pre}) of the tapered preamplifier, and the results are presented as the red triangles in Fig. 7. Note that for MOPA devices measured in Fig. 7, except the length and the type of the preamplifiers, all the other structure parameters are the same and the details are given in the caption. For each designed structure, two devices have been measured and the results are presented in Fig. 7, confirming perfect repeatability. Figure 7 illustrates when L_{pre} equals to 500 μm, devices with the straight or the tapered preamplifiers have nearly the same peak output power. It strongly indicates that the gain saturation is negligible when $L_{pre} \leq 500$ μm. In this case, the peak output power follows

$$P_{out} = P_{out,MO} \times \eta_{PA} = P_{out,MO} \times \exp(g \times L_{pre}) \times \kappa_{GC}. \tag{1}$$

Where $P_{out,MO}$ is the seed power from the MO section, η_{PA} the amplification factor of the PA section. κ_{GC} is the coupling efficiency, measuring the radiation power extracted from the grating coupler normalized by the power injected into it. From the peak output power of devices in which $L_{amp} \leq 500$ μm, we have deduced the values of g, κ_{GC}, and P_{MO} with the assistance of numerical simulations. We assume that $P_{out,MO}$ and κ_{GC} keep constant because the devices have the same structure of the MO and the grating coupler. From the relationship between the total output power and the preamplifier length, the net material gain g is found to be ~25 cm^{-1}. Considering this deduced gain, the FEM simulations show that the coupling efficiency κ_{GC} is about 1.25. With these data, we can further deduce from Eq. (1) that the seed power is approximately 10.1 mW. With this deduced $P_{out,MO}$, the maximum amplification factor η_{PA} (obtained in the MOPA device with a 1500-μm-long tapered preamplifier) is about 13.5. The green curve in Fig. 7 plots the relationship between P_{out} and L_{pre} described by Eq. (1) with the deduced net gain and seed power. Figure 7 shows that, when $L_{pre} \geq 1000$ μm, P_{out} of MOPA devices with a tapered preamplifier are significantly larger than those with a straight preamplifier, but are still less than the values predicted by Eq. (1). It indicates that the tapered preamplifier reduces but does not completely overcome the gain saturation.

Up to now, the gain saturation is the main issue limiting the preamplifier length and thus the effect of power amplification. To further suppress the gain saturation, a tapered preamplifier with a larger taper angle is necessary. More importantly, the spreading of the THz wave should match the taper angle. The export of the MO section determines the emission aperture of the THz wave. The narrower the MO section, the more spread the THz beam in the preamplifier. Therefore, a lager taper angle requires a narrower MO section but it in turn limits the seed power. In order to further improve the output power and the beam directionality of the MOPA devices, it is very necessary to optimize the seed power, the beam spreading in the preamplifier, and the coupling efficiency of the grating coupler.

5. Conclusions

High power THz-MOPA-QCLs have been demonstrated by improving the seed power from the MO section, suppressing the residue reflection from the grating coupler, and reduce the gain saturation in the preamplifier. The output power of the THz-MOPA-QCLs is more than one order of magnitude higher than the FP and the second-order DFB lasers fabricated from the same material. Our work points out a direction for the realization of single-mode THz-QCLs with high output power and good beam quality.

In our MOPA device, instead of high quality AR multilayers, a grating coupler together with an absorbing boundary exhibits extremely low reflectivity and high efficiency of power extraction. Thanks to the scalability of the Maxwell equations, the MOPA architecture developed in this work can be utilized in mid- and near-IR semiconductor lasers, and also in detectors and amplifiers for free space light radiation.

Funding

National Natural Science Foundation of China (61574149, 61734006); The Key Project of Chinese National Programs for Research and Development (2016YFB0402303, 2016YFA0202200); “The Hundred Talents Program” of CAS; The Engineering and Physical Sciences Research Council (EPSRC), UK (COTS programme EP/J017671/1); The Royal Society and Wolfson Foundation.

Acknowledgments

We thank Dr. Raffaele Colombelli for helpful discussions.